

Machine learning prediction of 2D perovskite photovoltaics and interaction with energetic ion implantation

Cite as: Appl. Phys. Lett. **119**, 231902 (2021); doi: [10.1063/5.0072745](https://doi.org/10.1063/5.0072745)

Submitted: 24 September 2021 · Accepted: 25 November 2021 ·

Published Online: 8 December 2021



View Online



Export Citation



CrossMark

Hong-Jian Feng^{a)} and Ping Ma

AFFILIATIONS

School of Physics, Northwest University, Xi'an 710127, China

^{a)} Author to whom correspondence should be addressed: hjfeng@nwu.edu.cn and fenghongjian@126.com

ABSTRACT

Atomic-level prediction combined with machine learning (ML) and density functional theory (DFT) is carried out to accelerate the fast discovery of potential photovoltaics from the 2D perovskites. Based on the ML prediction, stability test, optical absorption, and the theoretical power conversion efficiency (PCE) evaluation, two promising photovoltaics, i.e., Sr_2VON_3 and Ba_2VON_3 , are discovered with PCE as high as 30.35% and 26.03%, respectively. Cu, Ag, C, N, H, and He ion implantation are adopted to improve the photovoltaic performance of the high-efficiency and best stable perovskite Sr_2VON_3 . The time-dependent DFT electronic stopping calculations for energetic ion implanted Sr_2VON_3 indicate that the excited electrons from the valence band contribute to the electron–phonon coupling, the evolution and formation of the defects, and the photovoltaic performance. This work opens the way to the high-accuracy fast discovery of the high-efficiency and environmentally stable 2D perovskites solar cells and the further engineering improvement in photovoltaic performance by ion implantation.

Published under an exclusive license by AIP Publishing. <https://doi.org/10.1063/5.0072745>

Organic–inorganic hybrid perovskites solar cells have reached the record power conversion efficiency (PCE) of 25.5% that has never been achieved by the traditional solar cells in such a short period since the first endeavor of the perovskite cells.^{1–3} The excellent photovoltaic performance of the perovskites cells is ascribed to the optimal bandgap,^{4,5} the large optical absorption associated with its strong *p-p* transition across the band edge,^{6,7} the defect tolerance,^{8,9} and the higher carrier mobility and diffusion length associated with the strong band dispersion near the band edge.¹⁰ However, the large lattice constants and the vibration of the organic moieties render the decomposition of perovskites solar cells, the so-called the instability issue, which severely hinders further industrial application.¹¹ Thus, finding perovskite-type photovoltaic materials becomes the alternative way to solve the instability issue and the Pb-related toxic problem. For example, 32 A-site organic cations, 43 B-site divalent cations, and 4 X-site halogen ions are selected to build the 5504 perovskites prediction dataset,¹² the machine learning (ML) and density functional theory (DFT) have been combined to screen the potential perovskites solar materials. Six perovskites have been predicted with optimal bandgap and good dynamic stability. Except for the three-dimensional (3D) perovskites, the double perovskites, i.e., $\text{A}_2\text{B}^{1+}\text{B}^{3+}\text{X}_6$, have been another

alternative solution to the instability and toxic problem. Im *et al.* selected 540 double perovskites materials to predict the heat of formation (ΔH_f) and the bandgap (E_g).¹³ 3686 ABX_3 perovskites and 1509 $\text{A}_2\text{B}^{1+}\text{B}^{3+}\text{X}_6$ double perovskites materials in the Materials Projects (MP) are considered in a ML procedure to evaluate the formability of the 3D perovskites and double perovskites.¹⁴

Ruddlesden–Popper (RP) two-dimensional (2D) perovskites like $(\text{BA})_2(\text{MA})_2\text{Pb}_3\text{I}_{10}$ ($n = 3$) and $(\text{BA})_2(\text{MA})_3\text{Pb}_4\text{I}_{13}$ ($n = 4$) exhibit PCE of 12.5% with improved stability subject to light, humidity, and heat stress.¹⁵ The 2D $(\text{CH}_3(\text{CH}_2)_3\text{NH}_3)_2(\text{CH}_3\text{NH}_3)_{n-1}\text{Pb}_n\text{I}_{3n+1}$ ($n = 1, 2, 3$, and 4) perovskite light absorbing layer has also been synthesized, and the corresponding solar cells show good light and humidity stability after long exposure in the environment.¹⁶ Dion–Jacobson (DJ) 2D perovskite $(3\text{AMP})(\text{MA})_3\text{Pb}_4\text{I}_{13}$ has achieved the PCE of 7.32% and improved stability performance.¹⁷ RP 2D perovskites have the general formula as $\text{A}'_2\text{A}_{n-1}\text{B}_n\text{X}_{3n+1}$, while the DJ 2D perovskites have the form $\text{A}'\text{A}_{n-1}\text{B}_n\text{X}_{3n+1}$. A' ions in the DJ phase are divalent and those in the RP phase are monovalent; therefore, the inorganic layer in the latter case is displaced along in the plane.^{18–20} The stability improvement in the 2D perovskites is attributed to the organic layer, which acts as a capping layer and suppresses the decomposition of the inorganic

octahedron. At the same time, the side-effect is the decreased photovoltaic performance due to the inhibition of the carrier transport along the direction perpendicular to the organic layer. The directional carrier transport can be significantly alleviated if the organic layer is replaced by other inorganic ions, such as metal ions. Therefore, organic moieties can be substituted by other cations, and the same row elements can occupy A-site, B-site, and X site. That leads to a large class of layered perovskite materials. Indeed, this kind of layered perovskites can be found in the Computational Materials Repository (CMR) database.^{21–24} The prediction and screening of potential photovoltaic candidates from this large number of layered perovskites is beyond the DFT high-throughput computational capability. ML prediction from this class of 2D perovskites dataset is highly desirable and urgent in the current stage. The Voronoi tessellations method builds the corresponding Voronoi polyhedron of the nearest neighbor atoms and can reflect the structure and local environment of the crystals.^{25,26} We implemented the Voronoi tessellations scheme in our ML model to achieve an atomic level accuracy prediction from a large variety of different crystalline structure dataset.²⁷

Ion implantation has been widely used in biomaterials, alloys, and semiconductors modification.^{28–30} The optical absorption coefficient of the solar cell materials can be significantly improved by Cu ion implantation in our previous work.³¹ The implantation depth and range can be controlled by the accelerated voltage of the ion source while the damage formation and distribution is associated deeply with the implantation energy and fluence.³² The implanted ions experience energy loss from two kinds of interactions: One is the collision with the host atom, the so-called the nuclear stopping; the other is the retarding force ascribed to the electrons in the host materials, known as the electronic stopping.^{33,34} The latter interaction, i.e., the electron

stopping power (ESP), can be treated by the nonadiabatic way implemented in time-dependent density functional theory (TD-DFT).³⁵ Nuclear stopping power (NSP) and ESP are essential to understand the evolution and formation of the defects and the exciting process of the carriers during the ion implantation. The optical absorption coefficient of the ML predicted perovskites could be further improved by the ion implantation, which provides a way to design and improve the photovoltaic materials.

In this work, we used a gradient boosting regressor (GBR), an extra tree regressor (EXTR), and a random forest regressor (RF) algorithm-based ML method to train 2303 perovskites materials in the training dataset. The trained model has been used to screen further the 4828 materials, which have already been prescreened by the DFT structural relaxation validation from the original 29 285 artificial perovskites. DFT calculations have been used further to validate the stability, the optical absorption, and the theoretical PCE. Ion implantation has been used to improve the optical absorption of the best perovskite candidate, i.e., Sr_2VON_3 .

Figure 1 shows the flow chart of our screening process. It mainly composes the dataset construction, ML algorithms, and DFT calculation validation. There exist three types of perovskites in the input training dataset, i.e., the 2D perovskites, the 3D perovskites, and the double perovskites, which, respectively, contain 539, 271, and 1493 materials from the CMR database. 41 potential perovskites are adopted as the initial structure to construct the prediction dataset by artificially replacing the corresponding element. After obtaining the crystal structure and the bandgap of the training dataset, we used the Materials Agnostic Platform for Informatics and Exploration (Magpie) platform to obtain 271 initial features. Meanwhile, the Voronoi tessellation

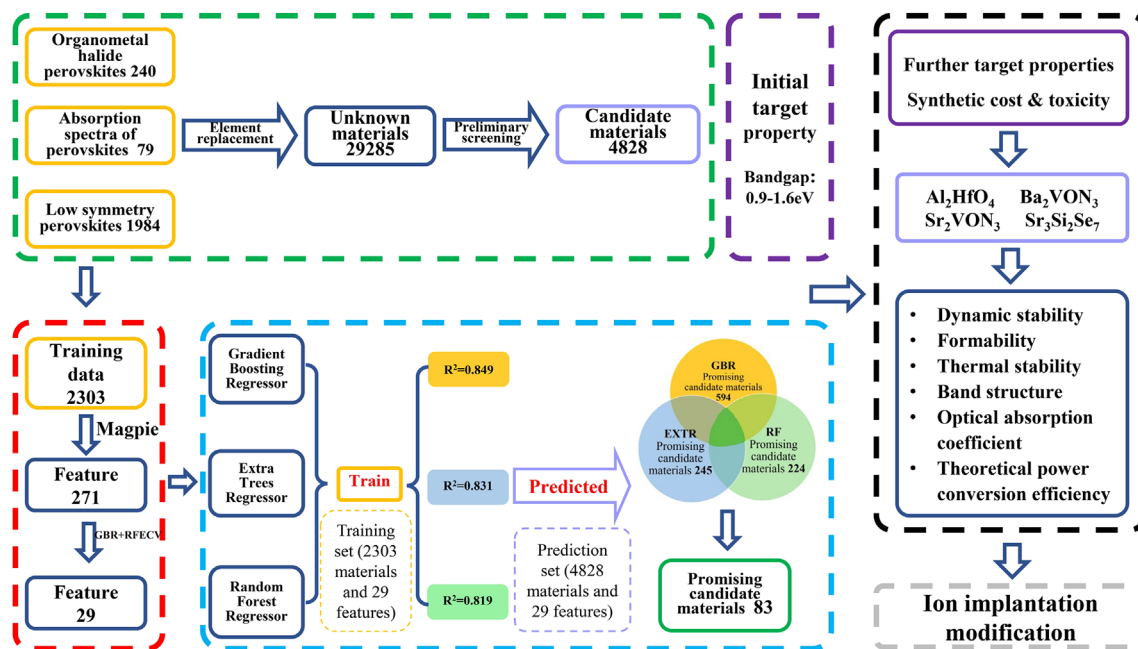


FIG. 1. A design framework for predicting perovskite photovoltaic materials based on ML and DFT calculations. The left part shows the working process of ML, which starts with the preparation and processing of data (green box) and then performs feature engineering (red box) based on target property (purple box). Then, the ML model is trained to screen the prediction dataset (blue box). The right part shows further validation of the predicted materials (black box). Ion implantation is used to improve the optical properties of the ideal perovskite (gray box).

method and recursive feature elimination cross validation (RFECV) method are, respectively, used to generate the attributes and remove redundant features, avoiding the curse of dimensionality. The target bandgap we chosen is 0.9–1.6 eV.

The space group and crystal structure of the materials in the training and prediction datasets are shown in Figs. 2(a) and 2(b). The dataset is divided into the training set (80%) and the test set (20%) to train the model. We selected 29 285 materials as the initial prediction

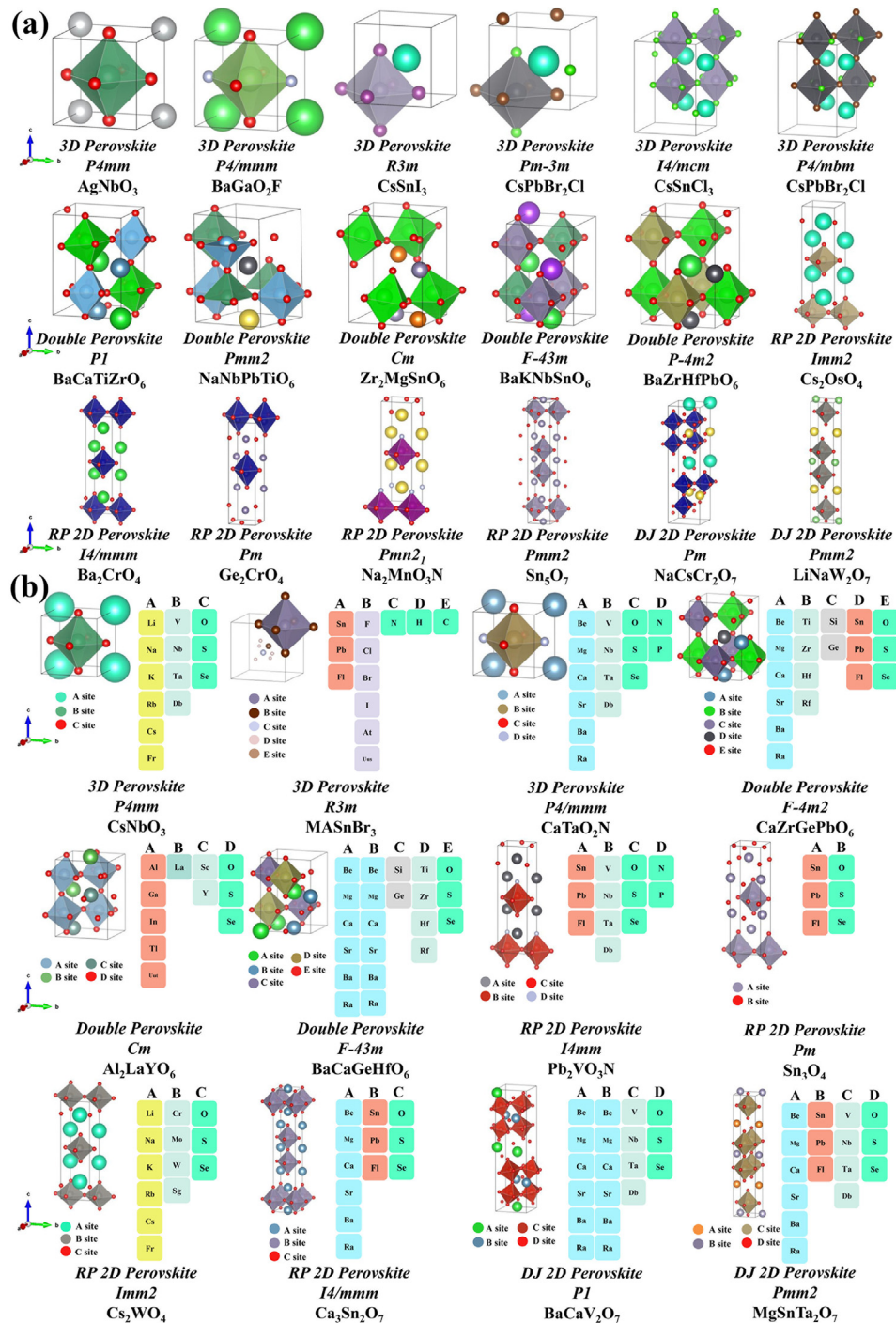


FIG. 2. The representative crystal structures and the space group for (a) the perovskites training dataset and (b) the prediction dataset.

dataset after removing the well-known solar cell materials and 4828 perovskites as the prediction dataset by screening the structural relaxation. The criterion to pass the relaxation is given in the [supplementary material](#).

Figures 3(a) and 3(b), respectively, show the ranking of feature importance and the whole list of the 29 features based on the GBR algorithm. The three features with the largest weight are the key attributes for our ML prediction and can be understood by the following physical features: (1) the average Warren-Cowley ordering parameters of the key network defined by the Voronoi polyhedron; (2) the DFT calculated ground state volume per atom at $T = 0$ K; and (3) the number of unfilled d valence orbitals. It can be seen that the correlation between most of the features is very small in the correlation heat map of 29 features as shown in Fig. 3(c), suggesting that the mainly selected features are not related and that we have removed redundant features,

which is very beneficial to improve the performance of the GBR model. In our ML prediction, the three algorithms, GBR, EXTR, and RF, are implemented, and if passing three model predictions simultaneously, the candidates can enter the next step evaluation. The coefficient of determination (R^2) for GBR, EXTR, and RF reached 0.849, 0.831, and 0.819, respectively. From Fig. 3(d), the R^2 , MSE, and MAE of the training dataset from the GBR model are 0.849, 0.49, and 0.43, respectively. The corresponding results for EXTR and RF models are shown in Figs. S1 and S2. Figure 3(e) shows the distribution of bandgap calculated from the DFT method and predicted by the three models. GBR, EXTR, and RF models predicted 594, 245, and 224 promising photovoltaics, respectively. Finally, 83 candidates with a suitable bandgap are obtained according to the screening rules mentioned above. The radiative element-related perovskites in the 83 candidates will be excluded from further DFT evaluation due to its

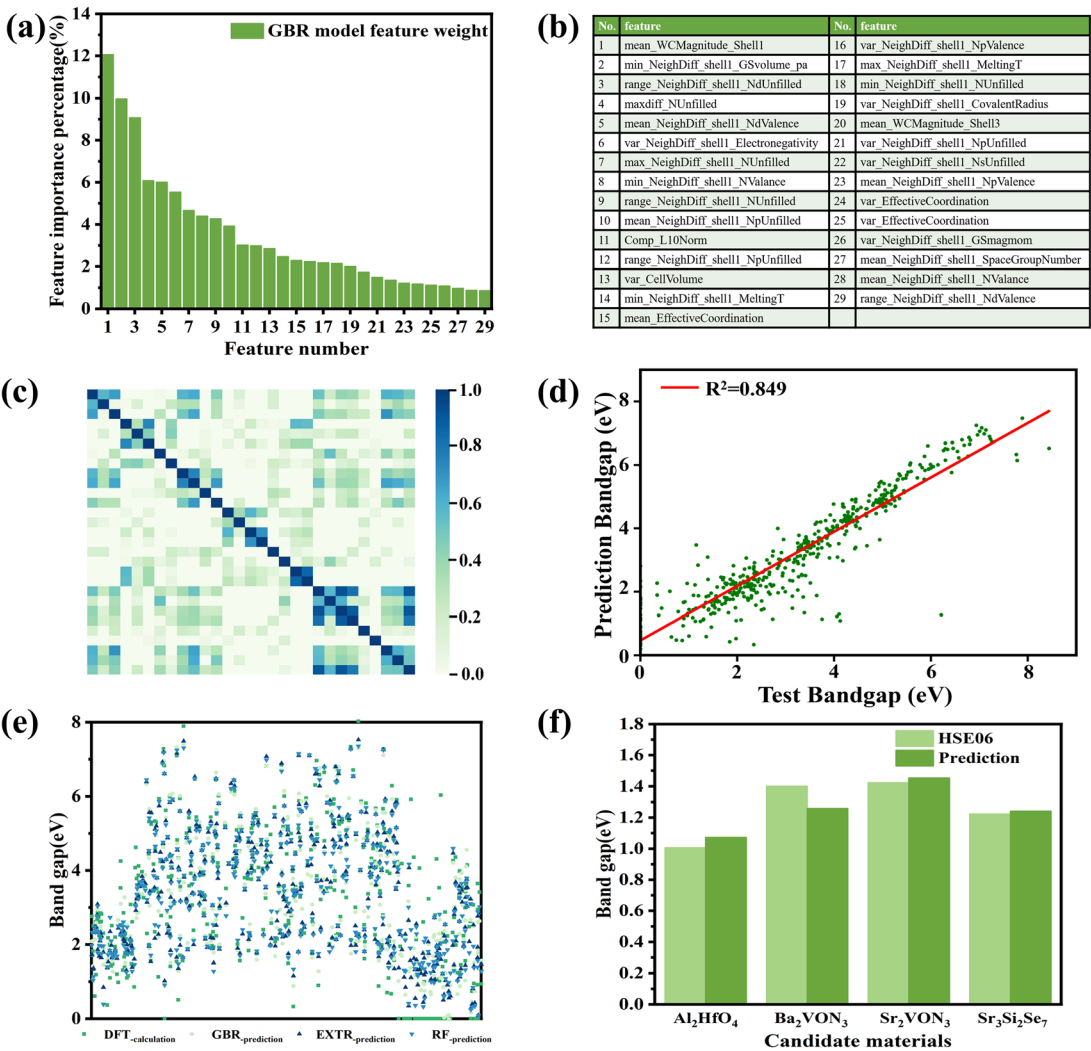


FIG. 3. Evaluation of the ML model. (a) The ranking of importance and (b) the whole list of 29 features in the GBR model. (c) A heat map of the correlation between 29 features with an absolute value. (d) The prediction results of the GBR model for the training dataset. (e) The bandgap distribution for DFT calculated value, GBR, EXTR, and RF model. (f) The comparison of the bandgap for the four predicted materials between ML prediction and HSE06 DFT calculations.

radiative behavior and serious threat to human health. Further screening from the 83 candidates is conducted based on the price, the toxicity, and radiation of the precursor and the elements in the candidates. Therefore, there are eight candidates left after the screening, and only four candidates with the optimum bandgap (0.9–1.6 eV) will be further evaluated by DFT calculations in the next section. Figure 3(f) shows the consistency of the average band gaps between the ML prediction and the DFT calculation, suggesting the atomic level accuracy of our ML prediction.

Four RP 2D perovskites, i.e., Al_2HfO_4 , Ba_2VON_3 , Sr_2VON_3 , and $\text{Sr}_3\text{Si}_2\text{Se}_7$, are predicted to be potential photovoltaics. They belong to three space groups: (1) Al_2HfO_4 (*Imm2*, No.44); (2) Ba_2VON_3 and Sr_2VON_3 (*I4mm*, No.107); and (3) $\text{Sr}_3\text{Si}_2\text{Se}_7$ (*I4/mmm*, No.139). The corresponding lattice constants are listed in Table S1. *Ab initio* molecular dynamic (AIMD) simulations under the constant-pressure Nosé–Hoover dynamics NPT ensemble have been performed to evaluate the dynamic stability of the four candidates. As shown in Figs. 4(a)–4(c), the energy variation of Al_2HfO_4 , Ba_2VON_3 , and Sr_2VON_3 supercell is very small, and the total energy curve is nearly flat, showing the relatively stable structure of these three materials. The peak around 1.05 ps of the total energy curve for $\text{Sr}_3\text{Si}_2\text{Se}_7$ indicates structural instability (see Fig. S3); meanwhile, the structure of Ba_2VON_3 exhibits a slight distortion at ~ 1300 fs, as shown in Fig. 4(b). The trivial atomic distortions 2D perovskites imply the stability of the initial

structure. To further test the formability, we calculated the decomposition enthalpy (ΔH_d) of the four materials concerning all the possible decomposition pathways, and the results for the most possible three decomposition pathways are shown in Fig. 4(d). However, all the possible decomposition pathways for these four materials are given in Fig. S4. The negative value of ΔH_d indicates that the predicted perovskite structure is thermally stable. Two materials, i.e., Ba_2VON_3 and Sr_2VON_3 , are thermodynamically stable; meanwhile, the positive ΔH_d value for Al_2HfO_4 and $\text{Sr}_3\text{Si}_2\text{Se}_7$ exhibits the possible decomposition pathway, showing the instability in the environmental condition. The two environmentally stable and the two unstable materials are shown in Fig. 4(e). Therefore, the dynamic and thermodynamic tests exclude two unstable structures, leaving only two stable materials, i.e., Ba_2VON_3 and Sr_2VON_3 .

The phonon dispersion was adopted further to validate the dynamic and structural stability, and the phonon dispersion curves with respect to the high symmetry points are shown in Figs. 4(f) and 4(g). It can be seen that both Ba_2VON_3 and Sr_2VON_3 have no imaginary frequency, which means that all the possible soft modes have been suppressed in the predicted structures and further confirms the excellent environmental stability. Specially, the pseudo soft modes at X point in low frequency regions may indicate the potential phase transitions and instability [Figs. 4(f) and 4(g)]. Moreover, from the band structures (Fig. S5) and density of states (DOS, see Fig. S6), it can be

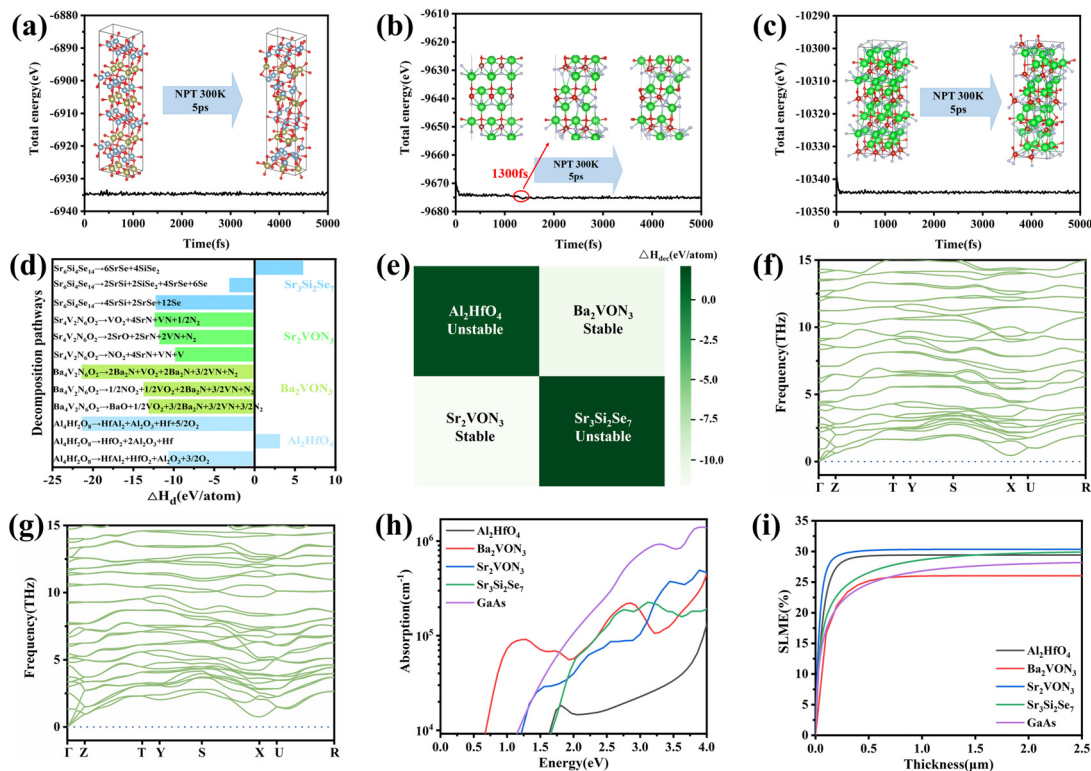


FIG. 4. The dynamic stability, environmental formability, and the calculated PCE of the candidate materials. Variation of the total energy of AIMD simulations for (a) Al_2HfO_4 , (b) Ba_2VON_3 , and (c) Sr_2VON_3 . (d) The decomposition enthalpy corresponds to the three maximum energy decomposition pathways of the four candidates. (e) The stable and the unstable states for the predicted four materials. The low frequency regions of the phonon dispersion spectrum of (f) Ba_2VON_3 and (g) Sr_2VON_3 . (h) The absorption spectra for Al_2HfO_4 , Ba_2VON_3 , Sr_2VON_3 , $\text{Sr}_3\text{Si}_2\text{Se}_7$, and GaAs. (i) SLME within the Shockley-Queisser model for Al_2HfO_4 , Ba_2VON_3 , Sr_2VON_3 , $\text{Sr}_3\text{Si}_2\text{Se}_7$, and GaAs at 300 K.

concluded that the effective mass of electron is 1.3 and 0.2 for Ba_2VON_3 and Sr_2VON_3 and the latter has the improved carrier mobility and charge dissociation ability for being used as solar cells. From the photon absorption spectra [Fig. 4(h)] and the spectroscopic limited maximum efficiency [SLME, see Fig. 4(i)], we can see that the absorption coefficients of the four ML predicted materials are in the same order of magnitude as the champion solar cell GaAs, meaning that the four predicted materials show good light absorption characteristics in the visible light range and confirming the atomic level accuracy of our ML prediction. This large optical absorption coefficient is ascribed to the optical transition probability across the band edge. Moreover, one can find that the theoretical PCE of Al_2HfO_4 and $\text{Sr}_3\text{Si}_2\text{Se}_7$, respectively, are 29.42% and 30.04% and when the film thickness is approaching 700 nm, the theoretical PCE approximately reaches the saturation value. Considering the large theoretical PCE 30.35% for Sr_2VON_3 and 26.03% for Ba_2VON_3 , we can see them as the high-efficiency and environmentally stable solar cell materials. The DFT computational details about the theoretical PCE can be found in our previous work^{27,31} and the related literature.³⁶ We found that the Si-ON_3 -related materials have already been synthesized.³⁷ This is an indication of the possible synthesis of our predicted ON_3 -related materials,

which have the same ON_3 group. Considering the deviation ($\sim 5\%$) of experimental PCE (25.5%) from the theoretical PCE ($\sim 30.5\%$)^{38,39} for perovskite MAPbI_3 , we expect the experimentally optimized PCE of Sr_2VON_3 -based perovskite solar cells to be $\sim 25\%$.

The high-efficiency environmentally stable perovskite Sr_2VON_3 is chosen as the ideal photovoltaic material for further ion implantation modification. In order to further improve the optical absorption of Sr_2VON_3 , Cu, Ag, C, N, H, and He, lower energy ion implantation has been adopted to improve the optical response. We used molecular dynamic (MD) simulation to determine the defects type when the kinetic energy of the implanted ion is lower enough (<1 eV) during the ion implantation process. The energy variation of the implanted ion is shown in Fig. 5(a). The stable defects type is determined to be interstitials, rather than the vacancies or replacements. Thus, we used the interstitial defects to calculate the DOS and optical absorption coefficient for ion implanted Sr_2VON_3 .

Ion implantation breaks structural symmetry and further changes the electronic states. The total DOS and partial DOS of Sr_2VON_3 without implantation and C ion implantation are shown in Fig. 5(b), and the DOS of Sr_2VON_3 implanted with Ag and Cu ion can be seen in Fig. S7. Figure 5(c) shows the absorption coefficient of the pristine

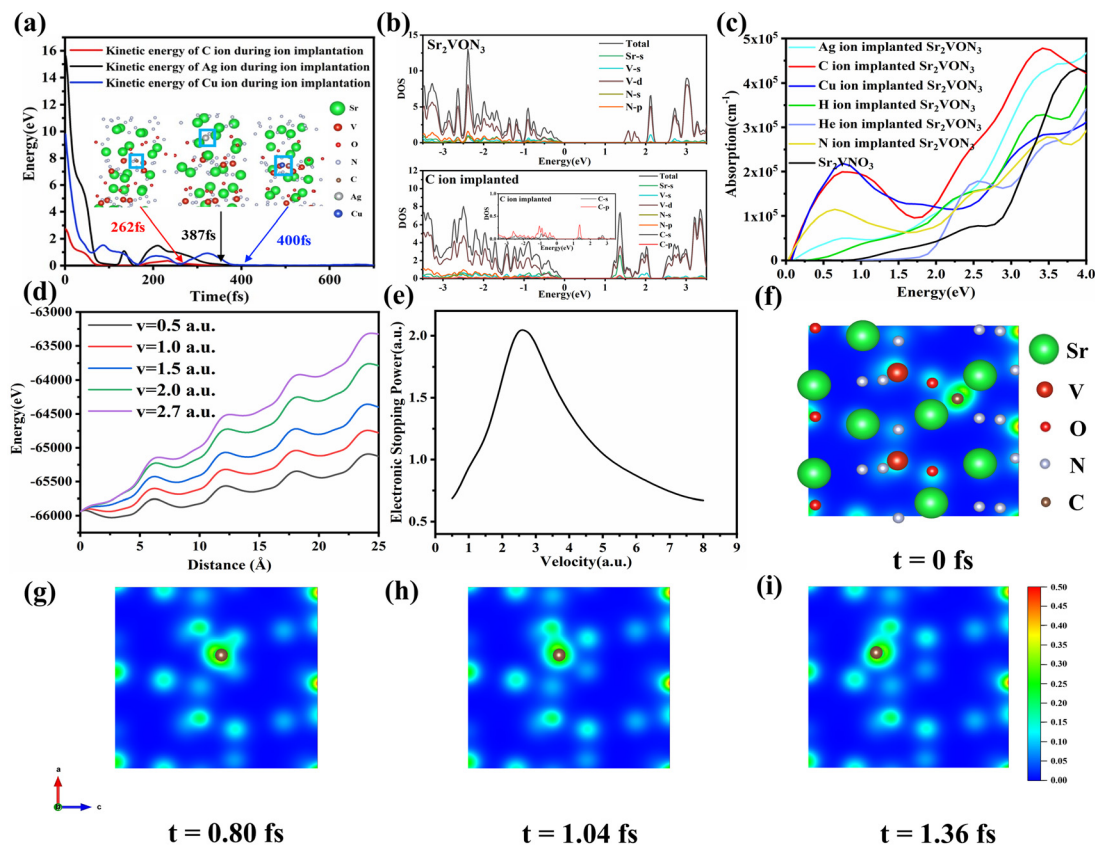


FIG. 5. The ion implantation modification, ESP, and the electronic excitation of Sr_2VON_3 . (a) Evolution of the kinetic energy of the implanted Ag, C, and Cu ion in the host matter. (b) The density of states of the pristine Sr_2VON_3 and the case after C ion implantation. (c) The optical absorption of the pristine Sr_2VON_3 and the case after ion implantation. (d) The electronic energy of the host material as a function of the trajectory distance of C ion with different ion implantation velocities. (e) The ESP of Sr_2VON_3 as a function of velocity of the projectile. The TDDFT charge density evolution at (f) $t = 0$ fs, (g) $t = 0.8$ fs, (h) $t = 1.04$ fs, and (i) $t = 1.36$ fs as C ion intruding through Sr_2VON_3 .

Sr_2VON_3 and the ion implanted cases. Indeed, all the six-ion implantation improves the absorption coefficient significantly in the visible light region, showing that the ion implantation would be an effective way to further improve the photovoltaic performance of the ML predicted Sr_2VON_3 . Among them, the C and Cu implantation renders the most photovoltaic performance enhancement. The enhanced optical absorption is ascribed to the occurrence of the state across the band edge induced by the implanted ions [see Fig. 5(b)]. In order to get a deeper understanding of the defect evolution and the carrier excitation during the C ion implantation, we choose C ion as the intruding ion to study the ESP. The variation of electronic energy of the host material as a function of distance traveled by the intruding ion is illustrated in Fig. 5(d). Thus, the ESP is calculated as the energy loss per unit distance of the intruding ion traveled along the implantation direction, and the corresponding ESP is shown in Fig. 5(e). For the semiconductor material, the valence electrons in the host material are excited from the valence band to the conduction band when the projectile passes through the host matter and experiences the retarding force from host matter. Therefore, there exists a threshold velocity of the ESP for projectile, intruding through the semiconductor. The interaction becomes complex in this case because the excited electrons will correlate with the host atom and the projectile at same time. The implanted ion will interact with the host nuclei, and the latter will impact on the motion of the projectile; thus, the interaction becomes nonadiabatic during the ion implantation process. Therefore, TD-DFT calculation was carried out to investigate the nonadiabatic interaction through the electron-phonon coupling. The electron response during the ion implantation process is capable of describing the carrier dynamics. The charge response for C passing through at 0, 0.8, 1.04, and 1.36 femtosecond is shown in Figs. 5(f)–5(i), respectively. The charge response at other time is reported in Fig. S8. It can be seen that the wake around the projectile C ion is exactly attributed to the valence band excitation, and the excited carrier definitely renders the complicated retarding force experienced by the implanted ions, which influences further the projectile ion track and the defects formation and evolution during the ion implantation process. This effect will give rise to the change in perovskite solar cell performance.

Three ML algorithms combined with DFT calculations were used to predict the promising photovoltaics from the 2D perovskites database. The four predicted materials, i.e., Al_2HfO_4 , $\text{Sr}_3\text{Si}_2\text{Se}_7$, Sr_2VON_3 , and Ba_2VON_3 , possess theoretical PCE as large as 29.42%, 30.04%, 30.35%, and 26.03%, respectively. Based on the phonon dispersion and decomposition enthalpy analysis, Ba_2VON_3 and Sr_2VON_3 were predicted to be the most environmentally stable and high-efficiency photovoltaic materials. After ion implantation, the optical absorption coefficient of Sr_2VON_3 was significantly improved; meanwhile, the ESP result for the C ion implantation in Sr_2VON_3 indicates that the excited valence electrons in the 2D perovskite and the projectile would influence the defects formation and the photovoltaic performance.

See the [supplementary material](#) for computational details, the ranking of importance of 29 features and the prediction results of EXTR and RF, variation of the total energy of AIMD simulations for $\text{Sr}_3\text{Si}_2\text{Se}_7$, the lattice parameters and decomposition energy path of the four candidate materials, the band structure and DOS for Ba_2VON_3 and Sr_2VON_3 , the DOS for Ag and Cu implantation, and the evolution of charge density of C implanted Sr_2VON_3 .

This work was financially supported by the National Natural Science Foundation of China (NSFC) under Grant Nos. 51972266, 51672214, 11304248, and 11247230 and the Fund Program for the Scientific Activities of Selected Returned Overseas Professionals in Shaanxi Province of China.

AUTHOR DECLARATIONS

Conflict of Interest

The authors declare no conflicts of interest.

DATA AVAILABILITY

The data that support the findings of this study are available from the corresponding author upon reasonable request.

REFERENCES

- A. Filippetti and A. Mattoni, "Hybrid perovskites for photovoltaics: Insights from first principles," *Phys. Rev. B* **89**, 125203 (2014).
- J. Jeong, M. Kim, J. Seo, H. Lu, P. Ahlawat, A. Mishra, Y. Yang, M. A. Hope, F. T. Eickemeyer, M. Kim, Y. J. Yoon, I. W. Choi, B. P. Darwich, S. J. Choi, Y. Jo, J. H. Lee, B. Walker, S. M. Zakeeruddin, L. Emsley, U. Rothlisberger, A. Hagfeldt, D. S. Kim, M. Grätzel, and J. Y. Kim, "Pseudo-halide anion engineering for α -FAPbI₃ perovskite solar cells," *Nature* **592**, 381 (2021).
- See <https://www.nrel.gov/pv/cell-efficiency.html> for "Best Research-Cell Efficiency Chart" (NREL, last accessed July 26, 2021).
- M. G. Ju, J. Dai, L. Ma, and X. C. Zeng, "Perovskite chalcogenides with optimal bandgap and desired optical absorption for photovoltaic devices," *Adv. Energy Mater.* **7**, 1700216 (2017).
- M. G. Ju, J. Dai, L. Ma, and X. C. Zeng, "Lead-free mixed tin and germanium perovskites for photovoltaic application," *J. Am. Chem. Soc.* **139**, 8038 (2017).
- Y. Q. Zhao, B. Liu, Z. L. Yu, J. M. Ma, Q. Wan, P. B. He, and M. Q. Cai, "Strong ferroelectric polarization of $\text{CH}_3\text{NH}_3\text{GeI}_3$ with high-absorption and mobility transport anisotropy: Theoretical study," *J. Mater. Chem. C* **5**, 5356 (2017).
- A. Onton, "Optical absorption due to excitation of electrons bound to Si and S in GaP," *Phys. Rev.* **186**, 786 (1969).
- T. H. Han, S. Tan, J. L. Xue, L. Meng, J. W. Lee, and Y. Yang, "Interface and defect engineering for metal halide perovskite optoelectronic devices," *Adv. Mater.* **31**, 1803515 (2019).
- F. Granberg, K. Nordlund, M. W. Ullah, K. Jin, C. Lu, H. Bei, L. M. Wang, F. Djurabekova, W. J. Weber, and Y. Zhang, "Mechanism of radiation damage reduction in equiatomic multicomponent single phase alloys," *Phys. Rev. Lett.* **116**, 135504 (2016).
- M. Puppini, P. Polishchuk, N. Colonna, A. Crepaldi, D. N. Dirin, O. Nazarenko, R. De Gennaro, G. Gatti, S. Roth, T. Barillot, L. Poletto, R. P. Xian, L. Rettig, M. Wolf, R. Ernstorfer, M. V. Kovalenko, N. Marzari, M. Grioni, and M. Chergui, "Evidence of large polarons in photoemission band mapping of the perovskite semiconductor CsPbBr_3 ," *Phys. Rev. Lett.* **124**, 206402 (2020).
- A. K. Paul, M. Reehuis, V. Ksenofontov, B. Yan, A. Hoser, D. M. Többsen, P. M. Abdala, P. Adler, M. Jansen, and C. Felser, "Lattice instability and competing spin structures in the double perovskite insulator $\text{Sr}_2\text{FeOsO}_6$," *Phys. Rev. Lett.* **111**, 167205 (2013).
- S. Lu, Q. Zhou, Y. Ouyang, Y. Guo, Q. Li, and J. Wang, "Accelerated discovery of stable lead-free hybrid organic-inorganic perovskites via machine learning," *Nat. Commun.* **9**, 3405 (2018).
- J. Im, S. Lee, T.-W. Ko, H. W. Kim, Y. Hyon, and H. Chang, "Identifying Pb-free perovskites for solar cells by machine learning," *npj Comput. Mater.* **5**, 37 (2019).
- Q. Xu, Z. Li, M. Liu, and W. J. Yin, "Rationalizing perovskite data for machine learning and materials design," *J. Phys. Chem. Lett.* **9**, 6948 (2018).
- H. Tsai, W. Nie, J. C. Blancon, C. C. Stoumpos, R. Asadpour, B. Harutyunyan, A. J. Neukirch, R. Verduzco, J. J. Crochet, S. Tretiak, L. Pedesseau, J. Even, M. A. Alam, G. Gupta, J. Lou, P. M. Ajayan, M. J. Bedzyk, and M. G. Kanatzidis, "High-efficiency two-dimensional Ruddlesden-Popper perovskite solar cells," *Nature* **536**, 312 (2016).

- ¹⁶D. H. Cao, C. C. Stoumpos, O. K. Farha, J. T. Hupp, and M. G. Kanatzidis, "2D homologous perovskites as light-absorbing materials for solar cell applications," *J. Am. Chem. Soc.* **137**, 7843 (2015).
- ¹⁷L. Mao, W. Ke, L. Pedesseau, Y. Wu, C. Katan, J. Even, M. R. Wasielewski, C. C. Stoumpos, and M. G. Kanatzidis, "Hybrid Dion-Jacobson 2D lead iodide perovskites," *J. Am. Chem. Soc.* **140**, 3775 (2018).
- ¹⁸Y. Zhang, J. Wang, and P. Ghosez, "Unraveling the suppression of oxygen octahedra rotations in $A_3B_2O_7$ Ruddlesden-Popper compounds: Engineering multi-ferroicity and beyond," *Phys. Rev. Lett.* **125**, 157601 (2020).
- ¹⁹S. Ahmad, P. Fu, S. Yu, Q. Yang, X. Liu, X. Wang, X. Wang, X. Guo, and C. Li, "Dion-Jacobson phase 2D layered perovskites for solar cells with ultrahigh stability," *Joule* **3**, 794 (2019).
- ²⁰T. Birol, N. A. Benedek, and C. J. Fennie, "Interface control of emergent ferroic order in Ruddlesden-Popper $Sr_{n+1}Ti_nO_{3n+1}$," *Phys. Rev. Lett.* **107**, 257602 (2011).
- ²¹I. E. Castelli, J. M. García-Lastra, F. Hüser, K. S. Thygesen, and K. W. Jacobsen, "Stability and bandgaps of layered perovskites for one-and two-photon water splitting," *New J. Phys.* **15**, 105026 (2013).
- ²²I. E. Castelli, K. S. Thygesen, and K. W. Jacobsen, "Bandgap engineering of double perovskites for one-and two-photon water splitting," *Mater. Res. Soc. Symp. Proc.* **1523**, 706 (2013).
- ²³See <https://cmr.fysik.dtu.dk> for "Computational Materials Repository."
- ²⁴I. E. Castelli, K. S. Thygesen, and K. W. Jacobsen, "Calculated optical absorption of different perovskite phases," *J. Mater. Chem. A* **3**, 12343 (2015).
- ²⁵L. Ward, A. Agrawal, A. Choudhary, and C. Wolverton, "A general-purpose machine learning framework for predicting properties of inorganic materials," *npj Comput. Mater.* **2**, 16028 (2016).
- ²⁶L. Ward, R. Liu, A. Krishna, V. I. Hegde, A. Agrawal, A. Choudhary, and C. Wolverton, "Including crystal structure attributes in machine learning models of formation energies via Voronoi tessellations," *Phys. Rev. B* **96**, 024104 (2017).
- ²⁷H.-J. Feng, K. Wu, and Z.-Y. Deng, "Predicting inorganic photovoltaic materials with efficiencies >26% via structure-relevant machine learning and density functional calculations," *Cell Rep. Phys. Sci.* **1**, 100179 (2020).
- ²⁸G. Dearnaley, "Ion implantation," *Nature* **256**, 701 (1975).
- ²⁹J. A. Davies, G. Foti, L. M. Howe, J. B. Mitchell, and K. B. Winterbon, "Polyatomic-ion implantation damage in silicon," *Phys. Rev. Lett.* **34**, 1441 (1975).
- ³⁰T. Herrmannsdörfer, V. Heera, O. Ignatchik, M. Uhlarz, A. Mücklich, M. Posselt, H. Reuther, B. Schmidt, K. H. Heinig, W. Skorupa, M. Voelskow, C. Wündisch, R. Skrotzki, M. Helm, and J. Wosnitzer, "Superconducting state in a gallium-doped germanium layer at low temperatures," *Phys. Rev. Lett.* **102**, 217003 (2009).
- ³¹H.-J. Feng and Q. Zhang, "Predicting efficiencies >25% A_3MX_3 photovoltaic materials and Cu ion implantation modification," *Appl. Phys. Lett.* **118**, 111902 (2021).
- ³²P. G. Coleman and C. P. Burrows, "Monovacancy and interstitial migration in ion-implanted silicon," *Phys. Rev. Lett.* **98**, 265502 (2007).
- ³³W. D. Wilson, L. G. Haggmark, and J. P. Biersack, "Calculations of nuclear stopping, ranges, and straggling in the low-energy region," *Phys. Rev. B* **15**, 2458 (1977).
- ³⁴M. Backman, F. Djurabekova, O. H. Pakarinen, K. Nordlund, Y. Zhang, M. Toulemonde, and W. J. Weber, "Cooperative effect of electronic and nuclear stopping on ion irradiation damage in silica," *J. Phys. D: Appl. Phys.* **45**, 505305 (2012).
- ³⁵D. C. Yost, Y. Yao, and Y. Kanai, "Examining real-time time-dependent density functional theory nonequilibrium simulations for the calculation of electronic stopping power," *Phys. Rev. B* **96**, 115134 (2017).
- ³⁶L. Yu and A. Zunger, "Identification of potential photovoltaic absorbers based on first-principles spectroscopic screening of materials," *Phys. Rev. Lett.* **108**, 068701 (2012).
- ³⁷X. Zhang, Z. Liu, Z. Zheng, S. Hark, Y. Fu, and G. Zhang, "Synthesis and photoluminescence properties of well-aligned Ga-doped N-rich SiO_xN_y nanowire bundles," *Appl. Phys. Lett.* **90**, 183110 (2007).
- ³⁸X.-G. Zhao, D. Yang, Y. Sun, T. Li, L. Zhang, L. Yu, and A. Zunger, "Cu-In halide perovskite solar absorbers," *J. Am. Chem. Soc.* **139**, 6718 (2017).
- ³⁹L. M. Pazos-Outón, T. P. Xiao, and E. Yablonovitch, "Fundamental efficiency limit of lead iodide perovskite solar cells," *J. Phys. Chem. Lett.* **9**, 1703 (2018).